Synthesis and characterisation of fluorescent and biocompatible hydroxyapatite nanoparticles with cerium doping

Wenjie Huang[1], Zhou Mao[1], Li Chen[1], Yuling Chi[1], Hao Jiang[1], Bhahat Lawlley Zimba[1], Guoxi Xiong[2] ✉, Qingzhi Wu[1]

[1]*State Key Laboratory of Advanced Technology for Materials Synthesis and Processing, Biomedical Material and Engineering Center, Wuhan University of Technology, Wuhan 430070, People's Republic of China*
[2]*Technology Center of China Tobacco Hubi Industrial Co. Ltd, Wuhan 430040, People's Republic of China*
✉ *E-mail: xionggx@hbtobacco.cn*

Published in Micro & Nano Letters; Received on 10th October 2017; Revised on 19th December 2017; Accepted on 2nd February 2018

In this work, the fluorescent hydroxyapatite nanoparticles (HA NPs) were synthesised by doping cerium (Ce) ions into the crystal structure of HA at different concentrations. The fluorescent property of the Ce-doped HA NPs was determined by the content of Ce doping. The results show that HA NPs with the Ce-doping content of 5% displayed the highest fluorescent emission peak near 380 nm at the excitation wavelength of 300 nm. The CCK-8 assay showed that no significant cytotoxicity was observed when the L929 cells were incubated with the fluorescent HA NPs with the Ce-doping content of 5% for 12 h at the dose lower than 0.1 mg/ml. Therefore, the fluorescent HA NPs could be used as a fluorescent probing for cellular imaging and antioxidant agent against oxidative stress-induced cell damages.

1. Introduction: Hydroxyapatite (HA, $Ca_{10}(PO_4)_6(OH)_2$) is the principal inorganic component of vertebrate skeleton particularly in bone, cartilage, enamel, and dentin, as well as the most stable calcium phosphate phase at physiological pH environment [1, 2]. Biologically, mineralised HA crystal is usually in hexagonal structure that is accompanied by high degree of substitutions. For example, both OH^- and PO_4^{3-} in HA crystal could be replaced by CO_3^{2-} particularly in bone and teeth, resulting in the formation of A-type and B-type carbonated HA [3]. On the other hand, Ca^{2+} in HA crystal could also be replaced by other monovalent or bivalent ions, such as K^+, Na^+, Mg^{2+}, Sr^{2+}, Ba^{2+}, Mn^{2+}, Zn^{2+}, and REE^{3+} (rare-earth elements) [4–6]. It has been shown that half of the elements in the periodic table could be incorporated into HA crystal structure, which paves the way to synthesise a series of HA derivatives. Therefore, HA nanoparticles (NPs) with excellent biocompatibility display promising potentials in biomedical fields, including artificial bone, tissue engineering scaffolds, biological probing, anticancer and antibacterial reagents, and drug delivery system [7–12].

Cerium (Ce) and its oxides have been demonstrated to have promising applications in biomedical fields. Studies have shown the excellent antibacterial activities of CeO_2 and Ce-doping composites [13, 14]. A transformation between Ce^{3+} and Ce^{4+} has been attributed to the redox enzyme-mimicking activities of CeO_2 nanostructures. This implies that CeO_2 nanostructures could be used as anti-oxidative agents against oxidative stress-induced damages in various cells and organs [15–19]. CeO_2 NPs have also been illustrated to stimulate proliferation of primary mouse embryonic fibroblasts through reduction of intracellular levels of reactive oxygen species (ROS) during the lag phase of cell growth and by modulating the expression level of the major antioxidant enzymes [20, 21]. On the other hand, CeO_2 and Ce-doping composites have been widely used as probing agents for fluorescent imaging and biosensors due to their excellent fluorescent properties under ultraviolet (UV) excitation [22–25]. Thus, Ce-doped HA nanostructures could be employed as a multifunctional agent for in vivo imaging and therapy of ROS damage-related diseases.

In our previous studies, a facile strategy has been developed for the tunable synthesis of HA nanostructures (NPs, nanorods, and microspheres) based on the supersaturation of the reaction system [26]. In this work, Ce-doped HA NPs were synthesised at different Ce-doping contents according to our previous synthesis strategy. The as-synthesised samples were characterised by transmission electron microscopy (TEM) and high-resolution TEM (HRTEM), X-ray diffraction (XRD), Fourier-transform infrared spectroscopy (FTIR), UV–visible (UV–Vis) and fluorescent spectra. Furthermore, the biocompatibility of Ce-doped HA NPs was evaluated by the CCK-8 assay in vitro using L929 cells as the model.

2. Materials and methods

2.1. Materials: Sodium tripolyphosphate ($Na_5P_3O_{10}$, STTP), calcium hydroxide ($Ca(OH)_2$), and cerium nitrate hexahydrate ($Ce(NO_3)_3{\cdot}6H_2O$) were of analytical grade (Sinopharm. Chemical Reagent Co., Ltd). All reagents were used as received without further purification. Deionised water (16 MΩ cm) was obtained from a Nanopure Water Systems UV (Thomas Scientific, Swedesboro, NJ).

2.2. Synthesis of Ce-doped HA NPs: In a typical synthesis, $Ca(OH)_2$ (4.1677 g, 56.2473 mmol) was dissolved in 45 ml of deionised water, then $Ce(NO)_3{\cdot}6H_2O$ (0.2432 g, 0.56 mmol) was added and dissolved in the $Ca(OH)_2$ solution (solution A). STTP (4.1308 g, 11.2293 mmol) was dissolved in another 45 ml of deionised water (solution B). Solution A was added dropwise to solution B at a constant rate (1 ml/min) under vigorous stirring at room temperature. The total (Ca + Ce)/P molar ratio of the reaction system was 1.67. After 1 h of stirring, the mixture was transferred and sealed into a 50 ml Teflon-lined stainless steel autoclave and heated to 180°C for 10 h and then cooled to room temperature. The precipitate was collected and washed alternately with ethanol and deionised water by centrifugation (9000 rpm for 5 min), and then dried at 60°C in the air. In a series of syntheses, the concentration of the reactants was adjusted as listed in Table 1.

2.3. Characterisations of the samples: The phase structure of the samples was identified by powder XRD on a D8 Advance diffractometer using Cu Kα radiation ($\lambda = 1.5418$ Å) at a scan speed of 0.5 s/step (increment = 0.05). The morphology and structure of the samples were observed using TEM (Tecnai G220, FEI Corp., The Netherlands) and HRTEM (JEM-2100F STEM/EDS, JEOL Corp, Japan), coupled with electron probe

microscopy (JXA-8230, Japan) for energy dispersive spectrometry analysis. The average size of the samples was analysed by counting at least 100 particles from scanning electron microscopy images using a software (Image J). FTIR spectra of the samples were recorded using FTIR (Nexus, Thermo Nicolet, America). The chemical composition and chemical state of the samples were analysed using inductively coupled plasma spectra (Optima 4300DV, PerkinElmer, America) and X-ray photoelectron spectroscopy (XPS) spectra (PHI Quantera II, ULVAC-PHI, Japan). UV–Vis spectra were recorded on a UV–Vis spectrophotometer (UV-2550 PC, Shimadzu Corp., Kyoto, Japan). The emission spectra of the samples were recorded on a fluorescence spectrophotometer (970CRT, SANCO, China).

3. Results and discussion: Fig. 1 shows TEM and HRTEM images of the as-synthesised HA NPs at different Ce-doping contents.

Table 1 Concentrations of the reagents used for the synthesis of Ce-doped HA NPs

No.	$Ce(NO_3)_3{\cdot}6H_2O$, mmol	$Ca(OH)_2$, mmol	STTP, mmol	Ce/(Ce + Ca) (molar ratio)
S0	0	0.6250	0.1248	0
S1	0.0062	0.6188	0.1248	1%
S2	0.0312	0.5938	0.1248	5%
S3	0.0625	0.0562	0.1248	10%
S4	0.1250	0.5000	0.1248	20%

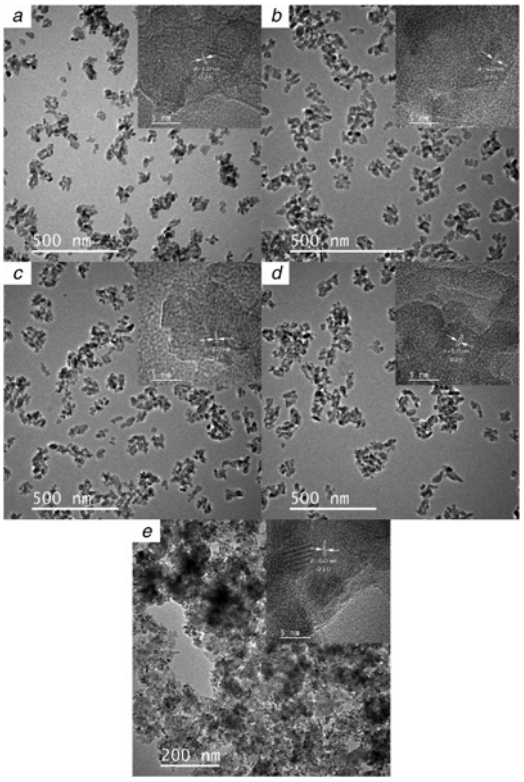

Fig. 1 *TEM and HRTEM images of as-synthesised samples*
a Pure HA NPs
b 1% Ce-doped HA NPs
c 5% Ce-doped HA NPs
d 10% Ce-doped HA NPs
e 20% Ce-doped HA NPs
The insets in TEM images show the HRTEM images of the as-synthesised samples. The spacing distance between the adjacent planes was marked with white lines

Fig. 1*a* shows the TEM image of HA NPS without Ce doping. Monodispersed HA NPs with the rice-like shape were obtained at an average length of ~37.6 ± 2.3 nm and an average width of ~19.3 ± 1.2 nm. The well-aligned crystal planes were observed from HRTEM image (the inset in Fig. 1*a*), implying the single crystal structure of the as-synthesised HA NPs. The interplanar spacing of ~0.23 nm obtained from the HRTEM image could be indexed to the adjacent (221) planes of HA crystal. Monodispersed Ce-doped HA NPs were obtained without significant changes in the shape and size (Figs. 1*b–d*). The average length and width were ~30.8 ± 2.1 and 18.8 ± 1.4 nm, 36.1 ± 1.8 and 19.9 ± 1.4 nm, 39.3 ± 2.3 and 21.5 ± 1.6 nm, corresponding to the Ce doping content of 1, 5, and 10%, respectively. However, HA NPs with serious aggregations were obtained by further increasing the Ce-doping content to 20%. The well-aligned crystal planes were observed from HRTEM images of Ce-doped HA NPs at different Ce contents (insets in Figs. 1*b–e*), implying the single crystal structure of the Ce-doped HA NPs. The interplanar spacing of ~0.23 nm obtained from the HRTEM images of the as-synthesised Ce-doped HA NPs could be indexed to the adjacent (221) planes of HA crystal. These results suggest that doping with Ce ions did not significantly alter the crystal structure of HA probably due to the similar ion radius of Ce^{3+} and Ca^{2+} (0.103 versus 0.099 nm) in HA crystal.

The incorporation of Ce ions into the HA crystal lattices was confirmed by energy-dispersive X-ray (EDX) spectra of the as-synthesised samples. As shown in Fig. 2*a*, all the characteristic peaks were assigned to the Ca, P, and O elements contained in HA crystal, while the peaks assigned to the C and Cu elements were derived from the carbon-coated Cu grids. As shown in Figs. 2*b–e*, the characteristic peaks assigned to the Ce element obviously appeared in EDX spectra of the Ce-doped samples. Moreover, the peak strength assigned to the Ce element

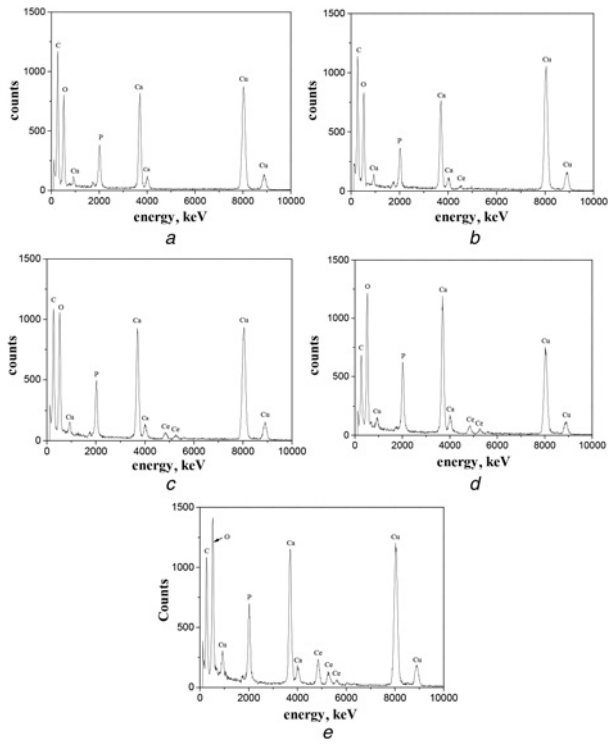

Fig. 2 *EDX spectra of the as-synthesised samples*
a Pure HA NPs
b 1% Ce-doped HA NPs
c 5% Ce-doped HA NPs
d 10% Ce-doped HA NPs
e 20% Ce-doped HA NPs

doi: 10.1049/mnl.2017.0729

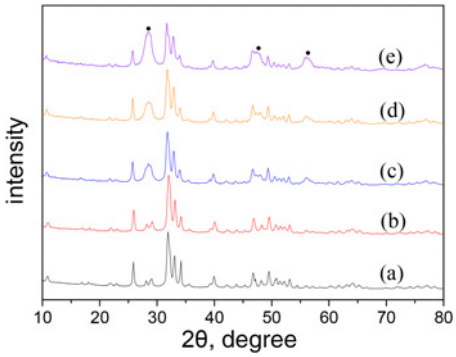

Fig. 3 *XRD patterns of the as-synthesised samples*
a Pure HA NPs
b 1% Ce-doped HA NPs
c 5% Ce-doped HA NPs
d 10% Ce-doped HA NPs
e 20% Ce-doped HA NPs. The diffraction peak derived from CeO_2 in XRD pattern was marked with black dots

significantly increased with the enhancement of the Ce content in the HA crystal. These results indicate that Ce ions were successfully incorporated into the HA lattices.

Fig. 3 shows XRD patterns of the as-synthesised HA NPs at different Ce-doping contents. All of the diffraction peaks in Fig. 3*a* could be indexed to hexagonal HA crystal (JCPDS Card No. 73-0293), indicating that the pure HA NPs were obtained in the absence of Ce doping. No obvious changes in diffraction peaks were observed in the case of 1% Ce doping (Fig. 3*b*), which could be attributed to the Ce doping content lower than the limit of detection by X-ray diffractometer. It is worth noting that two diffraction peaks ascribed to (102) and (210) planes of HA crystal were replaced by a stronger and broader peak in XRD patterns of the samples with the Ce-doping content higher than 5% (Figs. 3*c*–*e*), which could be attributed to the formation of CeO_2 [27]. The similar peak changes also appeared at (230) and (500) planes (~48.5° and 56.3° in the XRD patterns) (Figs. 3*c*–*e*).

Fig. 4 shows the FTIR spectra of the as-synthesised HA NPs at different Ce-doping contents. The peaks at 3450 and 1640 cm^{-1} in FTIR spectra were attributed to stretching and bending vibrations of O–H group in adsorbed water. Small shoulder peaks at 3570 and 620 cm^{-1} in Fig. 4*a* were attributed to stretching and bending vibrations of O–H group in HA crystal structure. The peaks at 1050 and 960 cm^{-1} were attributed to ν_3 and ν_1 stretching vibrations of PO_4^{3-}. The peaks at 600 and 570 cm^{-1} were attributed to

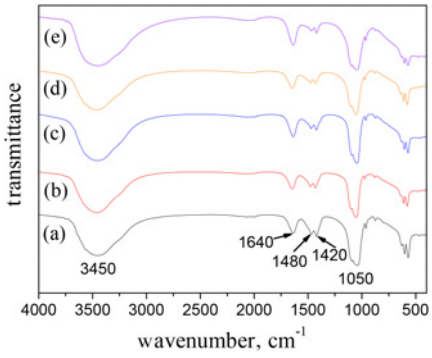

Fig. 4 *FTIR patterns of the as-synthesised samples*
a Pure HA NPs
b 1% Ce-doped HA NPs
c 5% Ce-doped HA NPs
d 10% Ce-doped HA NPs
e 20% Ce-doped HA NPs

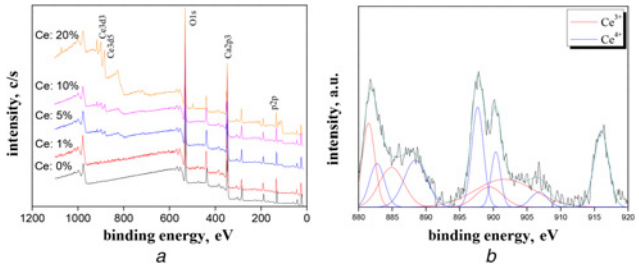

Fig. 5 *XPS spectra of the as-synthesised samples*
a XPS spectra of the as-synthesised samples
b Ce 3d XPS spectrum of the HA NPs with the Ce-doping content of 5%, which was fit to Ce^{3+} and Ce^{4+} chemical states and marked with red and blue lines, respectively

ν_1 stretching vibrations of PO_4^{3-} [27–29]. The decrease in peak strength derived from PO_4^{3-} was attributed to the substitution of Ce ions in HA crystal structure [27, 28]. It is noticeable that two peaks at 1480 and 1420 cm^{-1} were attributed to CO_3^{2-}, which was incorporated into the PO_4^{3-} sites and OH^- sites in HA crystal structure. These results indicate that the as-synthesised HA NPs were carbonated HA NPs.

The surface chemical state of the as-synthesised Ce-doped HA NPs was analysed by XPS characterisation. As shown in Fig. 5*a*, the binding energies assigned to the Ca2p, O1s, and P2p were detected in XPS spectra of the as-synthesised samples. The binding energy ranging from 880 to 920 eV was detected in the Ce-doped samples which were assigned to Ce3d. These results demonstrate the incorporation of Ce ions in the HA lattices. In order to further identify the chemical state of Ce ions contained in the Ce-doped HA NPs, the peaks in the range of 880–920 nm in the XPS spectra were fitted using the Gaussian function. Fig. 5*b* shows the fitting XPS spectra of the HA NPs with the Ce-doping content of 5%. Both Ce^{3+} and Ce^{4+} existed on the surface of the Ce-doped HA NPs. The presence of Ce^{4+} could be probably attributed to the oxidation of Ce^{3+} and the formation of CeO_2 in the surface of HA NPs. These results are in accordance with the XRD characterisation.

It is generally known that Ce ions display strong UV absorption and broad emission band due to its spin and parity allowed 4f–5d transitions [30, 31]. Fig. 6*a* shows the UV–Vis spectra of the as-synthesised HA NPs. No significant absorption was observed in UV–Vis spectrum of the pure HA NPs. A broad absorption near 300 nm was observed in UV–Vis spectra of Ce-doped HA NPs at the doping content from 5 to 20%. It is interesting that HA NPs with the Ce-doping content of 5% displayed higher UV absorption than HA NPs with the Ce-doping content of 10%. Fig. 6*b* shows the fluorescent emission spectra of the as-synthesised HA NPs at different Ce-doping contents at an excitation wavelength of 300 nm. A strong and broad maximum

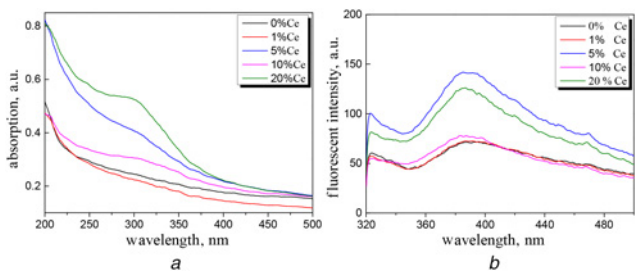

Fig. 6 *UV–Vis and fluorescent spectra of the as-synthesised samples*
a UV–Vis spectra of the as-synthesised samples
b Fluorescent spectra of the as-synthesised samples at the excitation wavelength of 300 nm

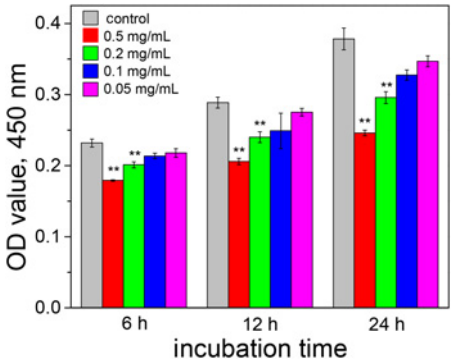

Fig. 7 *Cell viabilities of L929 cells incubated with HA NPs with the Ce-doping content of 5% at different time intervals and different doses*

emission peak near 380 nm was observed in HA NPs with the Ce-doping content of 5 and 20%. It is worth noting that the highest emission intensity was observed in HA NPs with the Ce-doping content of 5%. In addition, a weak shoulder peak was observed near 470 nm. Both of the two emission peaks could be assigned to 4f–5d transition of Ce^{3+} ions: 4f ($^2F_{5/2}$) → 5d ($^2B_{1g}$) and 4f ($^2F_{5/2}$) → 5d ($^2A_{1g}$), respectively [30, 31]. These results imply that Ce-doped HA NPs at the doping content of 5% could be used for cellular probing and imaging.

In order to evaluate the cytotoxicity of the fluorescent HA NPs with the Ce-doping content of 5%, L929 cells were used as the model and CCK-8 assay was carried out. As shown in Fig. 7, fluorescent HA NPs with the Ce-doping content of 5% were incubated with L929 cells at different doses for different time intervals. When L929 cells were incubated with the fluorescent Ce-doped HA NPs for 6 h, the cell viability was decreased to 77.3, 86.8, 92.2, and 94.0% compared with that of the control group, corresponding to the dose of 0.5, 0.2, 0.1, and 0.05 mg/ml, respectively. These results show that the fluorescent Ce-doped HA NPs significantly suppressed the proliferation of L929 cells at the dose higher than 0.1 mg/ml. When further extending the incubation time, the cell viability was 71.3, 83.2, 86.3, and 95.4% for 12 h, and 65.0, 78.3, 86., and 91.7% for 24 h, compared with that of the control group, corresponding to the dose of 0.5, 0.2, 0.1, and 0.05 mg/ml, respectively. These results show that the fluorescent Ce-doped HA NPs could be used as a fluorescent probing for cell imaging when the dose is lower than 0.1 mg/ml.

4. Conclusions: In summary, a series of fluorescent HA NPs were synthesised by doping Ce ions into the crystal structure of HA at different concentrations. The fluorescent property of the Ce-doped HA NPs was determined by the content of Ce doping. Among different Ce-doping contents, HA NPs with the Ce-doping content of 5% displayed the highest fluorescent emission peak near 380 nm at the excitation wavelength of 300 nm. The CCK-8 assay showed that although the fluorescent HA NPs with the Ce-doping content of 5% displayed the time- and dose-dependent cytotoxicity at the dose higher than 0.1 mg/ml, no significant cytotoxicity was observed when the cells were incubated with the fluorescent HA NPs for 12 h at the dose lower than 0.1 mg/ml. Therefore, the fluorescent HA NPs could be used as a fluorescent probing for cellular imaging and antioxidant agent against oxidative stress-induced cell damages.

5. Acknowledgment: This work was supported by the basic research project of Wuhan Science and Technology Bureau (grant no. 2014060101010041).

6 References

[1] Combes C., Rey C.: 'Amorphous calcium phosphates: synthesis, properties and uses in biomaterials', *Acta Biomat.*, 2010, **6**, (9), pp. 3362–3378
[2] Ginebra M.P., Espanol M., Montufar E.B., *ET AL.*: 'New processing approaches in calcium phosphate cements and their applications in regenerative medicine', *Acta Biomat.*, 2010, **6**, (8), pp. 2863–2873
[3] Omelon S.J., Grynpas M.D.: 'Relationships between polyphosphate chemistry, biochemistry and apatite biomineralization', *Chem. Rev.*, 2008, **108**, (11), pp. 4694–4715
[4] Yasukawa A., Gotoh K., Tanaka H., *ET AL.*: 'Preparation and structure of calcium hydroxyapatite substituted with light rare earth ions', *Colloid Surf. A*, 2012, **393**, (1), pp. 53–59
[5] Honda Y., Anada T., Morimoto S., *ET AL.*: 'Effect of Zn^{2+} on the physicochemical characteristics of octacalcium phosphate and its hydrolysis into apatitic phases', *Cryst. Growth Des.*, 2011, **11**, (5), pp. 1462–1468
[6] Dasgupta S., Banerjee S.S., Bandyopadhyay A., *ET AL.*: 'Zn- and Mg-doped hydroxyapatite nanoparticles for controlled release of protein', *Langmuir*, 2010, **26**, (7), pp. 4958–4964
[7] Yao C.L., Zhu J.M., Xie A.J., *ET AL.*: 'Graphene oxide and creatine phosphate disodium dual template-directed synthesis of GO/hydroxyapatite and its application in drug delivery', *Mater. Sci. Eng. C*, 2016, **73**, (1), pp. 709–715
[8] Vazquez-Hernandez F., Mendoza-Acevedo S., Mendoza-Barrera C.O., *ET AL.*: 'Antibody-coupled hydroxyapatite nanoparticles as efficient tools for labeling intracellular proteins', *Mater. Sci. Eng. C*, 2017, **71**, (1), pp. 909–918
[9] Xu J., Shen X.K., Jia L., *ET AL.*: 'Facile ratiometric fluorapatite nanoprobes for rapid and sensitive bacterial spore biomarker detection', *Biosens. Bioelectron.*, 2017, **87**, (1), pp. 991–997
[10] Wang F., Zhang Z.H.: 'Catalytic transfer hydrogenation of furfural into furfuryl alcohol over magnetic gamma-Fe_2O_3@HAP catalyst', *ACS Sustain. Chem. Eng.*, 2017, **5**, (1), pp. 942–947
[11] Zhang M., Liu J.K., Miao R., *ET AL.*: 'Preparation and characterization of fluorescence probe from assembly hydroxyapatite nanocomposites', *Nanoscale Res. Lett.*, 2010, **5**, pp. 675–679
[12] Jiang H., Liu J.K., Wang J.D., *ET AL.*: 'The biotoxicity of hydroxyapatite nanoparticles to the plant growth', *J. Hazard Mater.*, 2014, **270**, pp. 71–81
[13] Hui A.P., Liu J.L., Ma J.Z.: 'Synthesis and morphology-dependent antimicrobial activity of cerium doped flower-shaped ZnO crystallites under visible light irradiation', *Colloid Surf. A*, 2016, **506**, pp. 519–525
[14] Truffault L., Rodrigues D.F., Salgado H.R.N., *ET AL.*: 'Loaded Ce-Ag organic-inorganic hybrids and their antibacterial activity', *Colloid Surf. B*, 2016, **147**, pp. 151–160
[15] Singh R., Karakoti A.S., Self W., *ET AL.*: 'Redox-sensitive cerium oxide nanoparticles protect human keratinocytes from oxidative stress induced by glutathione depletion', *Langmuir*, 2016, **32**, (46), pp. 12202–12211
[16] Kim S.J., Chung B.H.: 'Antioxidant activity of levan coated cerium oxide nanoparticles', *Carbohyd. Polym.*, 2016, **150**, pp. 400–407
[17] Abbas F., Jan T., Iqbal J., *ET AL.*: 'Inhibition of neuroblastoma cancer cells viability by ferromagnetic Mn doped CeO_2 monodisperse nanoparticles mediated through reactive oxygen species', *Mater. Chem. Phys.*, 2016, **173**, pp. 146–151
[18] Guan Y.J., Li M., Dong K., *ET AL.*: 'Ceria/POMs hybrid nanoparticles as a mimicking metallopeptidase for treatment of neurotoxicity of amyloid-beta peptide', *Biomaterials*, 2016, **98**, (1), pp. 92–102
[19] Wahba S.M.R., Darwish A.S., Kamal S.M.: 'Ceria-containing uncoated and coated hydroxyapatite-based galantamine nanocomposites for formidable treatment of Alzheimer's disease in ovariectomized albino-rat model', *Mater. Sci. Eng. C*, 2016, **65**, pp. 151–163
[20] Popov A.L., Popova N.R., Selezneva I.I., *ET AL.*: 'Cerium oxide nanoparticles stimulate proliferation of primary mouse embryonic fibroblasts in vitro', *Mater. Sci. Eng. C*, 2016, **68**, pp. 406–413
[21] Yang Y.S., Mao Z., Huang W.J., *ET AL.*: 'Redox enzyme-mimicking activities of CeO_2 nanostructures: intrinsic influence of exposed facets', *Sci. Rep.*, 2016, **6**, p. 35344
[22] Zhu G.X., Zhao R.B., Li Y.L., *ET AL.*: 'Multifunctional Gd, Ce, Tb co-doped beta tricalcium phosphate porous nanospheres for sustained drug release and bioimaging', *J. Mater. Chem. B*, 2016, **4**, (22), pp. 3903–3910

doi: 10.1049/mnl.2017.0729

[23] Shehata N., Samir E., Gaballah S.: 'New optical sensor for peroxides using neodymium-doped-ceria nanoparticles via fluorescence-quenching technique', *Sens. Actuators B*, 2016, **231**, pp. 341–348
[24] Shehata N., Samir E., Gaballah S., *ET AL.*: 'Embedded ceria nanoparticles in crosslinked PVA electrospun nanofibers as optical sensors for radicals', *Sensors*, 2016, **16**, (9), p. 1371
[25] Xu Y.J., Lin J., Lu Y., *ET AL.*: 'Lanthanide co-doped paramagnetic spindle-like mesocrystals for imaging and autophagy induction', *Nanoscale*, 2016, **8**, (27), pp. 13399–13406
[26] Yang Y.S., Wu Q.Z., Wang M., *ET AL.*: 'Hydrothermal synthesis of hydroxyapatite with different morphologies: influence of supersaturation of the reaction system', *Cryst. Growth Des.*, 2014, **14**, (9), pp. 4864–4871
[27] Sun L.J., Guo D.G., Zhao W.A., *ET AL.*: 'Influences of reaction parameters and Ce contents on structure and properties of nano-scale Ce-HA powders', *J. Mater. Sci. Technol.*, 2014, **30**, (8), pp. 776–781
[28] Ciobanu G., Bargan A.M., Luca C.: 'New cerium (IV)-substituted hydroxyapatite nanoparticles: preparation and characterization', *Ceram. Int.*, 2015, **41**, (9), pp. 12192–12201
[29] Kaygili O., Dorozhkin S.V., Keser S.: 'Synthesis and characterization of Ce-substituted hydroxyapatite by sol-gel method', *Mater. Sci. Eng. C*, 2014, **42**, pp. 78–82
[30] Fang Z.J., Cao R.P., Zhang F.T., *ET AL.*: 'Efficient spectral conversion from visible to near-infrared in transparent glass ceramics containing Ce^{3+}-Yb^{3+} codoped $Y_3Al_5O_{12}$ nanocrystals', *J. Mater. Chem. C*, 2014, **2**, (12), pp. 2204–2211
[31] Yang C., Liang X.J., Di X.X., *ET AL.*: 'Facile fabrication and luminescence characteristics of Ce: YAG phosphor glass thick films coated on a glass substrate for white LEDs', *Ceram. Int.*, 2016, **42**, (13), pp. 14526–14532